

Evaluation of diagnostic pigments to estimate phytoplankton size classes

Alison P. Chase ^{1,*} Sasha J. Kramer,² Nils Haëntjens ¹ Emmanuel S. Boss ¹ Lee Karp-Boss ¹
Mimi Edmondson,¹ Jason R. Graff³

¹School of Marine Sciences, University of Maine, Orono, Maine

²Interdepartmental Graduate Program in Marine Science, University of California Santa Barbara, Santa Barbara, California

³Department of Botany and Plant Pathology, Oregon State University, Corvallis, Oregon

Abstract

Phytoplankton accessory pigments are commonly used to estimate phytoplankton size classes, particularly during development and validation of biogeochemical models and satellite ocean color-based algorithms. The diagnostic pigment analysis (DPA) is based on bulk measurements of pigment concentrations and relies on assumptions regarding the presence of specific pigments in different phytoplankton taxonomic groups. Three size classes are defined by the DPA: picoplankton, nanoplankton, and microplankton. Until now, the DPA has not been evaluated against an independent approach that provides phytoplankton size calculated on a per-cell basis. Automated quantitative cell imagery of microplankton and some nanoplankton, used in combination with conventional flow cytometry for enumeration of picoplankton and nanoplankton, provide a novel opportunity to perform an independent evaluation of the DPA. Here, we use a data set from the North Atlantic Ocean that encompasses all seasons and a wide range of chlorophyll concentrations (0.18–5.14 mg m⁻³). Results show that the DPA overestimates microplankton and picoplankton when compared to cytometry data, and subsequently underestimates the contribution of nanoplankton to total biomass. In contrast to the assumption made by the DPA that the microplankton size class is largely made up of diatoms and dinoflagellates, imaging-in-flow cytometry shows significant presence of diatoms and dinoflagellates in the nanoplankton size class. Additionally, chlorophyll *b* is commonly attributed solely to picoplankton by the DPA, but Chl *b*-containing phytoplankton are observed with imaging in both nanoplankton and microplankton size classes. We suggest revisions to the DPA equations and application of uncertainties when calculating size classes from diagnostic pigments.

Phytoplankton community composition, that is, the assemblage of different species present in the ocean, is variable in both time and space. Phytoplankton species span multiple taxonomic kingdoms and phyla, and several orders of magnitude in cell size (< 1 to > 1000 μm). Functional traits of phytoplankton communities have been applied as a way to study phytoplankton dynamics beyond bulk community measurements of biomass (e.g., chlorophyll *a* concentration [Chl *a*]), while reducing the need for collecting information on all individual species to a manageable and ecologically meaningful number

of groups (Le Quere and Harrison 2005; Litchman et al. 2010). Phytoplankton cell size is an important trait that influences nutrient uptake, growth rates, sinking rates, motility, and interactions with grazers (Litchman and Klausmeier 2008; Sommer et al. 2017). Three phytoplankton size classes (PSCs), originally defined by Sieburth et al. (1978), are commonly used in the classification of phytoplankton: picoplankton (0.2–2 μm), nanoplankton (2–20 μm), and microplankton (20–200 μm). Most literature addressing size classes uses < 2 μm and > 20 μm to define picoplankton and microplankton, respectively. These size classes follow from the observation of Sheldon et al. (1972) that the biomass of plankton in power-law increasing size bins is approximately equal. For brevity in this article, we indicate the three PSCs using the terms pico-, nano-, and microplankton without “phyto” included. There are some expected relationships between major phytoplankton taxonomic groups and the three size classes. For example, cyanobacteria from the genera *Synechococcus* and *Prochlorococcus* generally fall under

*Correspondence: alison.p.chase@maine.edu

Additional Supporting Information may be found in the online version of this article.

This is an open access article under the terms of the Creative Commons Attribution-NonCommercial-NoDerivs License, which permits use and distribution in any medium, provided the original work is properly cited, the use is non-commercial and no modifications or adaptations are made.

the operational definition of picoplankton (Chisholm 1992) (although we note that *Trichodesmium* colonies can reach microplankton size, or larger in some tropical and subtropical regions). Most cryptophytes are found in a relatively narrow range of sizes within the nanoplankton (Thronsdon 1997; Jeffrey et al. 2011). However, in some phytoplankton groups, such as diatoms and dinoflagellates, cell size spans a broad range from several to hundreds of micrometers. Knowledge of the distribution of phytoplankton cell sizes provides insights into ecosystem processes (e.g., carbon flux and nutrient cycling) and food web dynamics (namely grazer preferences and interactions) that are of importance in the ocean.

Efforts to observe and monitor the size structure of phytoplankton communities in the open ocean are limited by the challenges of in situ data collection. Satellite data allow quantification of PSCs on regional or global scales (e.g., Brewin et al. 2010; Hirata et al. 2011; Li et al. 2013; Roy et al. 2013; Kostadinov et al. 2009; see Mouw et al. 2017 for a review of recent literature). Development and validation of satellite algorithms requires extensive in situ data, but direct measurements of size-fractionated phytoplankton biomass are limited. Vidussi et al. (2001) proposed the use of phytoplankton pigment information measured by high-performance liquid chromatography (HPLC) analysis as an alternative to labor-intensive size-fractionated filtration and microscopy approaches. The rationale for this approach, which builds off of a method proposed by Claustre (1994) to estimate the relative abundance of microplankton, is that in addition to Chl *a*, phytoplankton contain various photosynthetic and photoprotective accessory pigments. Accessory pigments are associated with broad taxonomic phytoplankton groups as the result of multiple endosymbiosis events during the evolution of different eukaryotic algal lineages, as well as the evolution of photosynthetically active cyanobacteria (Jeffrey et al. 1997). Pigments contained within phytoplankton taxonomic groups are in turn assumed to be associated with one of the three size classes of pico-, nano-, and microplankton.

Vidussi et al. (2001) used seven diagnostic accessory pigments (fucoxanthin [Fuco], peridinin [Peri], 19'-hexanoyloxyfucoxanthin [Hexa], 19'-butanoyloxyfucoxanthin [Buta], alloxanthin [Allo], total chlorophyll *b* [TChl*b*], and zeaxanthin [Zea]) to derive PSCs. Generalizations must be made when assigning accessory pigments to phytoplankton taxonomic groups as well as taxa to each of the three size classes. The method of using diagnostic accessory pigments, referred to here as the diagnostic pigment analysis (DPA), was further developed by Uitz et al. (2006), who applied weighting coefficients to the same seven diagnostic pigments used by Vidussi et al. (2001) to describe the contribution of each PSC to total Chl *a*. The weighting coefficients were determined via multiple regression analyses comparing Chl *a* to the summed seven diagnostic pigments (Uitz et al. 2006). The reliance of the DPA on links between pigments and phytoplankton taxa (a separate

topic addressed with a variety of methods, e.g., Mackey et al. 1996; Kramer and Siegel 2019), as well as the size range of different phytoplankton taxonomic groups, is not trivial and requires further investigation.

Numerous works have revised the DPA equations to tune pigment weights to regional HPLC data sets and to reduce uncertainties resulting from the inherent assumptions of the method (Uitz et al. 2006, 2008; Hirata et al. 2008; Brewin et al. 2010, 2014, 2015, 2017; Devred et al. 2011; Sopha et al. 2014; Di Cicco et al. 2017; Gittings et al. 2019). Many other studies have directly applied published DPA equations and pigment weighting coefficients with no revision to equations (e.g., Hirata et al. 2011; Brotas et al. 2013; Organelli et al. 2013; Lorenzoni et al. 2015; Zeng et al. 2018). Brewin et al. (2014) evaluated the DPA using size-fractionated filtration and calculated PSCs using three published variations of the DPA. Their results showed that deviations in PSC estimates among the different DPA models are small compared to the deviations between the models and size-fractionated filtration. They also showed that the DPA tends to overestimate nanoplankton and underestimate picoplankton, compared to size-fractionated filtration. However, size-fractionated filtration does not cleanly separate particles of different size classes (Koestner et al. 2020), and with uncertainties in size-fractionated filtration not quantified in Brewin et al. (2014), the authors note that it is difficult to assess which of the two approaches (DPA and size-fractionated filtration) more accurately represents the size structure of the phytoplankton community. Brotas et al. (2013) fit the model of Brewin et al. (2010) to estimate Chl *a* concentrations per size class using bulk cell counts from cytometry and microscopy, and found results consistent with previous literature, but did not evaluate the biomass in size classes with phytoplankton size calculated on a per-cell basis. Previous efforts have also used DPA estimates as the in situ data to validate satellite algorithm results (Brewin et al. 2011) and as the baseline for evaluation of satellite-derived particle size distributions (Kostadinov et al. 2010). The ongoing application of DPA-based PSCs for describing the phytoplankton community, and perhaps even more importantly, as the in situ standard against which satellite-based PSC algorithms are compared, warrants a closer look at the assumptions and uncertainties of the DPA approach.

Despite the numerous revisions and applications of the DPA, an evaluation of the method using independent and more direct measurements of cell size has yet to be conducted. The DPA was originally intended to estimate Chl *a* concentrations within different size classes. However, its continued application in the literature to describe the phytoplankton community and the relative importance of pico-, nano-, and microplankton deems it appropriate for evaluation using the direct measurements of pico-, nano-, and microplankton biomass made possible with conventional and imaging flow

cytometry data. The lack of this type of evaluation to date is in large part the result of the labor-intensive task required to quantify cell size for a sufficiently large number of cells and samples. However, relatively recent advances in imaging-in-flow cytometry and its application to large-scale ocean studies via continuous flow-through data collection now enable this type of evaluation. Methods of quantifying cell size and size class Chl *a* fractions using cytometry are faced with a different set of challenges from those facing the DPA approach to quantifying cell sizes. Cytometry instruments require careful calibration against beads and/or phytoplankton cultures of known size to link scattering intensity or camera pixels to cell size. The nature of comprehensively enumerating or capturing images of individual cells means that cytometric instruments cannot sample large volumes of water. As a result, there are uncertainties in how well a few milliliters of water analyzed using cytometry represent the water mass where discrete samples on the order of 1–2 L of water have been collected for HPLC analysis.

In this study, we use a novel dataset of concurrently measured imaging-in-flow and conventional flow cytometry collected in the North Atlantic Ocean to evaluate the DPA. We compare DPA and cytometry-based estimates of phytoplankton biomass in the pico-, nano-, and microplankton size fractions of phytoplankton and assess uncertainties. Based on the results of our evaluation, we provide recommendations for revised DPA equations and application of uncertainties during implementation of the DPA in prospective studies.

Materials and procedures

Data used for evaluation of the DPA were collected as part of the North Atlantic Aerosol and Marine Ecosystems Study

(NAAMES). The study consisted of four research cruises in the western North Atlantic Ocean on the R/V *Atlantis* during November 2015 (NA01), May–June 2016 (NA02), August–September 2017 (NA03), and March–April 2018 (NA04). Locations of samples from the four cruises are shown in Fig. 1A. The study was designed to target different phases of the annual phytoplankton bloom spanning multiple seasons and a wide variety of water types (Fig. 1; Behrenfeld et al. 2019; Della Penna and Gaube 2019). Data presented here were collected both while the ship was “on-station” and during transit between stations and to and from port (Fig. 1A). All transit samples were collected from the ship’s continuous flowing seawater system (water intake at approximately 5 m depth), and on-station samples were either collected from the flowing seawater system or from the 5 m depth Niskin bottles that were deployed on a conductivity-temperature-depth (CTD) rosette.

HPLC pigment data and application of the DPA

Water samples (1–2 L) for HPLC pigment analysis were filtered onto precombusted (4 h, 450°C) 25 mm diameter Whatman GF/F filters with a nominal pore size of 0.7 μm precombustion and 0.3 μm postcombustion (Nayar and Chou 2003). Filters were stored in liquid nitrogen until analysis by the Ocean Ecology Laboratory at NASA Goddard Space Flight Center (GSFC) following the protocols described in Van Heukelem and Thomas (2001) and Hooker et al. (2009). Occasionally duplicate samples ($\sim 10\%$ of total samples per cruise) were collected by taking independent and consecutive water samples from the flowing seawater system. During HPLC analysis, mean and standard deviation (SD) values of pigment concentrations from replicates were calculated and the relative (%) coefficient of variation was used as the uncertainty of

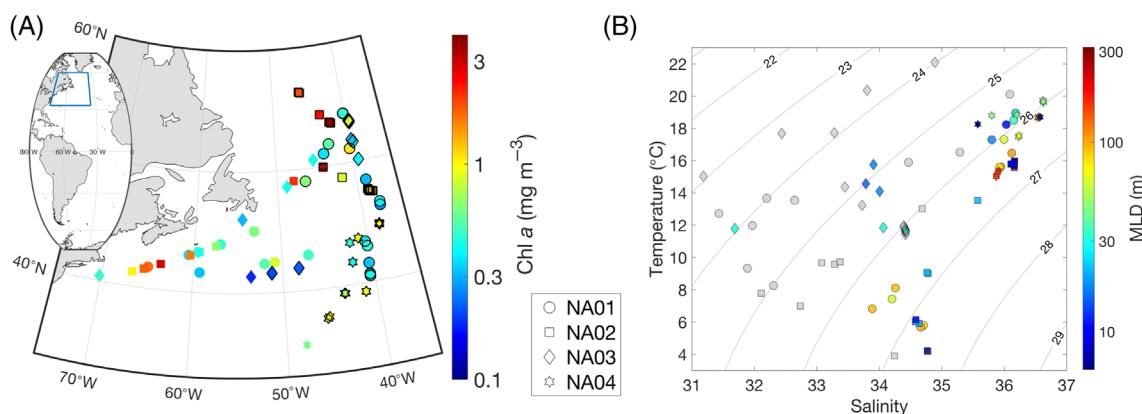


Fig 1. (A) Locations in the western North Atlantic of concurrently measured cytometry and HPLC data during four seasons (total $n = 90$): NAAMES 1 (November 2015, circles), NAAMES 2 (May–June 2016, squares), NAAMES 3 (August–September 2017, diamonds), and NAAMES 4 (March–April 2018, hexagrams). Samples are colored by their respective Chl *a* concentration, ranging from 0.18 to 5.14 mg m^{-3} (see Supporting Information Table S1 for values at each location). Symbols outlined with a black line represent samples from stations (vs. those collected during transit). **(B)** Temperature and salinity values associated with each of the 90 samples (legend follows the same convention as in panel A). Samples collected from stations are colored by mixed layer depth (MLD) values.

Table 1. Formulas to calculate picoplankton (F_p), nanoplankton (F_n), and microplankton (F_m) fractions from HPLC phytoplankton pigment concentrations as reported in previously published studies. Devred et al. (2011) and Hirata et al. (2008) apply equations from Uitz et al. (2006) for picoplankton and microplankton, respectively, and so are not shown here to avoid redundancy. DP_w = summed weighted diagnostic pigments (mg m^{-3}); $DP_w = \sum_{i=1}^7 W_i P_i$, where W = pigment weights (unitless; values shown in Table 2) and P = pigment concentrations (mg m^{-3}) = [Fuco(P_1), Peri(P_2), Hexa(P_3), Buta(P_4), Allo(P_5), TChlb(P_6), Zea(P_7)].

Formula	Reference	Equation
Picoplankton		
$F_p = \frac{\sum_{i=1}^7 W_i P_i}{DP_w}$	Uitz et al. (2006)	(1)
$F_p = \frac{W_7 P_7}{DP_w} + \text{all samples with Chl } a < 0.25 \text{ mg m}^{-3}$	Hirata et al. (2008)	(2)
Nanoplankton		
$F_n = \frac{\sum_{i=3}^5 W_i P_i}{DP_w}$	Uitz et al. (2006)	(3)
$F_n = \frac{\sum_{i=3}^6 W_i P_i}{DP_w}$	Hirata et al. (2008)	(4)
$F_n = \frac{(\sum_{i=3}^5 W_i P_i) + W_1 P_{1,n}}{DP_w}$ where $P_{1,n} = 10^{(0.531 \log_{10} P_3 + 0.708 \log_{10} P_4)}$	Devred et al. (2011)	(5)
Microplankton		
$F_m = \frac{\sum_{i=1}^2 W_i P_i}{DP_w}$	Uitz et al. (2006)	(6)
$F_m = \frac{(\sum_{i=1}^2 W_i P_i) - W_1 P_{1,n}}{DP_w}$ where $P_{1,n} = 10^{(0.531 \log_{10} P_3 + 0.708 \log_{10} P_4)}$	Devred et al. (2011)	(7)

HPLC-based Chl *a* in our analysis. Any pigment concentrations below the limit of detection were set to zero. To calculate PSCs from HPLC pigment concentrations, we applied all previously published versions of the DPA (Table 1 and references therein). We did not evaluate published relationships for very low chlorophyll concentrations ($< 0.08 \text{ mg m}^{-3}$), derived previously for ultraoligotrophic conditions by Brewin et al. (2010, 2014), as these conditions do not apply to our North Atlantic data set where Chl *a* concentrations at our sample locations ranged from 0.18 to 5.14 mg m^{-3} . We evaluated seven unique DPA equations (Table 1, Eqs. 1–7) after applying the seven diagnostic pigment weights (W) reported in Uitz et al. (2006) (Table 2). The same set of weights were applied in Hirata et al. (2008) and Devred et al. (2011). We also tested the impact of using different values for W by applying four previously published sets of W values for either global or North Atlantic data sets (Brewin et al. 2014, 2015, 2017; Soppa et al. 2014) (Table 2). Results for picoplankton (F_p), nanoplankton (F_n), and microplankton (F_m) fractions calculated using the four sets of W had SDs of 0.04, 0.02, and 0.02 (unitless fractions 0–1), respectively, therefore indicating that the results were not significantly changed by the application of different values of pigment weights. Additionally, we computed values of W from our dataset using a linear least-squares solver (MATLAB *lsqlin* function), and the summed weighted pigments showed strong correlation ($r = 0.97$) with HPLC-derived Chl *a* (Table 2). We tested the use of W values from our dataset in calculating PSCs and our results were not significantly changed. Contributions of each size class to total chlorophyll (Chl_p, Chl_n, Chl_m) were calculated by multiplying the size class fraction (F_p , F_n , F_m) by

Chl *a* concentration from HPLC analysis. We define Chl *a* as the sum of the concentrations of monovinyl Chl *a* + divinyl Chl *a* + chlorophyllide *a* + Chl *a* allomers and epimers as in Uitz et al. (2006).

Collection and analysis of cytometry data

Size measurements of individual phytoplankton cells were obtained from images collected with an Imaging FlowCytobot (IFCB; McLane Research Laboratories). The IFCB enumerates and images particles in the size range of ~ 6 –150 μm . The IFCB was calibrated with NIST-traceable size standard beads to determine the conversion from pixels to μm . The instrument was deployed in an automated in-line mode. Every ~ 20 min, 5 mL of seawater were drawn automatically from the ship's flow-through system. Cells and particles were individually imaged if a laser-induced chlorophyll fluorescence threshold was reached (Olson and Sosik 2007). The exact volume of water for each sample (mean = 4.8 mL, SD = 0.36 mL for our study) was recorded and applied during data analysis for quantification of cell concentrations. Images and associated metadata, as well as extracted features (Sosik and Olson 2007), were deposited on EcoTaxa, a web-based platform developed for the curation and annotation of plankton images (Picheral et al. 2017). Images were classified into taxonomic or functional group categories based on morphological features (images available at <https://ecotaxa.obs-vlfr.fr/>). Living cells were separated from nonliving particles and classification was completed to the highest taxonomic level possible based on instrument resolution and image characteristics. Cells lacking distinct morphological features are difficult to identify from

Table 2. Values of pigment weights (W) calculated in previous studies, and using the data of this study. Values of W are applied in Eqs. 1–7 (Table 1). Pearson’s linear correlation coefficient denoted by r . Note that the W values of this study are calculated for comparison, but values of Uitz et al. (2006) are used when evaluating published DPA equations.

Pigment	Uitz et al. (2006)	Brewin et al. (2014)	Soppa et al. (2014)	Brewin et al. (2015)	Brewin et al. (2017)	This study
Fucoxanthin (P_1)	1.41±0.02	1.72	1.554±0.01	1.51±0.01	1.65±0.01	2.62
Peridinin (P_2)	1.41±0.1	1.27	0.413±0.568	1.35±0.02	1.04±0.03	1.32
Hexa* (P_3)	1.27±0.02	0.68	0.855±0.068	0.95±0.01	0.78±0.01	0.87
Buta* (P_4)	0.35±0.15	1.42	1.174±0.145	0.85±0.35	1.19±0.03	0.0
Alloxanthin (P_5)	0.6±0.16	4.96	2.387±0.099	2.71±0.05	3.14±0.04	2.64
TChlb (P_6)	1.01±0.1	0.81	1.062±0.07	1.27±1.01	1.38±0.02	0.94
Zeaxanthin (P_7)	0.86±0.09	1.28	2.037±0.04	0.93±0.0	1.02±0.01	1.52
r between Chl a and ΣDP	0.76	0.965	0.85	0.98	0.99	0.97
# of data points	2419	466	3988	5841	2791	90
Geographical region	Global	North Atlantic, South Atlantic	Global	Global	North Atlantic	North Atlantic

*Hexa = 19'-hexanoyloxyfucoxanthin, Buta = 19'-butanoyloxyfucoxanthin.

IFCB images and were grouped under a category of “unidentifiable.” A learning set containing 14,917 manually validated images across 84 taxonomic or morphological (e.g., detritus) categories was applied in a random forest machine learning approach to predict the category of 250,660 images from IFCB samples across the four NAAMES cruises. All images used in this study were then manually confirmed or corrected in their category assignment. Following the export of information on classified particles from EcoTaxa, living cells were grouped into seven broad taxonomic categories: diatoms, dinoflagellates, silicoflagellates, prymnesiophytes, cryptophytes, euglenoids, chlorophytes, and “unidentifiable.” The only remaining living particles not included in these categories are the relatively rarely imaged ciliates and Rhizaria, which accounted for 2.3% of total cell biovolume. Nonliving particles including detritus, bubbles, and fecal pellets were removed from the analysis. Cell biovolumes were estimated following Moberg and Sosik (2012), from which the volume-based equivalent spherical diameter (ESD_V) of each cell was calculated. Estimates of cellular carbon for cells $> 7 \mu m$ were computed following equations in Menden-Deuer and Lessard (2000), and for cells $< 7 \mu m$ following Sommer et al. (2012).

An Influx Cell Sorter (ICS; BD Biosciences) was used to enumerate cells from discrete water samples collected with 5 m depth Niskin bottles or from the flow-through system. Samples were prefiltered through a $64 \mu m$ mesh filter prior to analysis to avoid clogging of the nozzle. A detailed description of the ICS set-up and operation used during NAAMES field campaigns can be found in Graff and Behrenfeld (2018). To quantitatively assess the size of ICS-measured particles, a two-step calibration was performed: (1) normalization of the forward scattering peak (FSC) measured by the ICS and (2) the conversion from normalized FSC to cell size. The FSC was normalized

for the gain sensitivity settings of the photomultipliers of the instrument and the alignment of the core of the flow with the laser. While the alignment of the flow must be done with precision beads used as a reference over time, the normalization to the gain settings of the photomultiplier tube can either be done with precision beads or a single culture (*Dunaliella* in our case) as it is done at one instant and is not time dependent. The FSC primarily depends on cell size (Gin et al. 1999; DuRand et al. 2001); however, it is also affected by the index of refraction and by particle shape. Therefore, we calibrated the ICS with cultures (see genera and species in Supporting Information Fig. S1). Sizing of cells from these cultures was also done with the IFCB within an hour of running the cultures on the ICS, with the exception of *Synechococcus* for which the size was estimated to be $1.15 \mu m$. The empirical relationship between size (ESD_V) and FSC that was obtained from the calibration (Supporting Information Fig. S1) was used to calculate the size of cells in the natural population samples. Size measurements from the ICS cover the range of approximately 0.5 – $20 \mu m$. Cell diameter was then used to calculate biovolumes (assuming spherical cells) and subsequently cellular carbon following Menden-Deuer and Lessard (2000) for cells $> 7 \mu m$ and Sommer et al. (2012) for cells $< 7 \mu m$.

Biovolume estimates of pico-, nano-, and microplankton from merged cytometry data

To calculate the pico-, nano-, and microplankton fractions from the combined IFCB and ICS data (henceforth we refer to the merged data from these two instruments as “cytometry”), we use ICS data for picoplankton ($< 2 \mu m$), IFCB data for microplankton (> 20 – $150 \mu m$), and a combination of the two data types for nanoplankton (2 – $20 \mu m$). To do so, for each sample, we plotted the particle size distribution from the IFCB

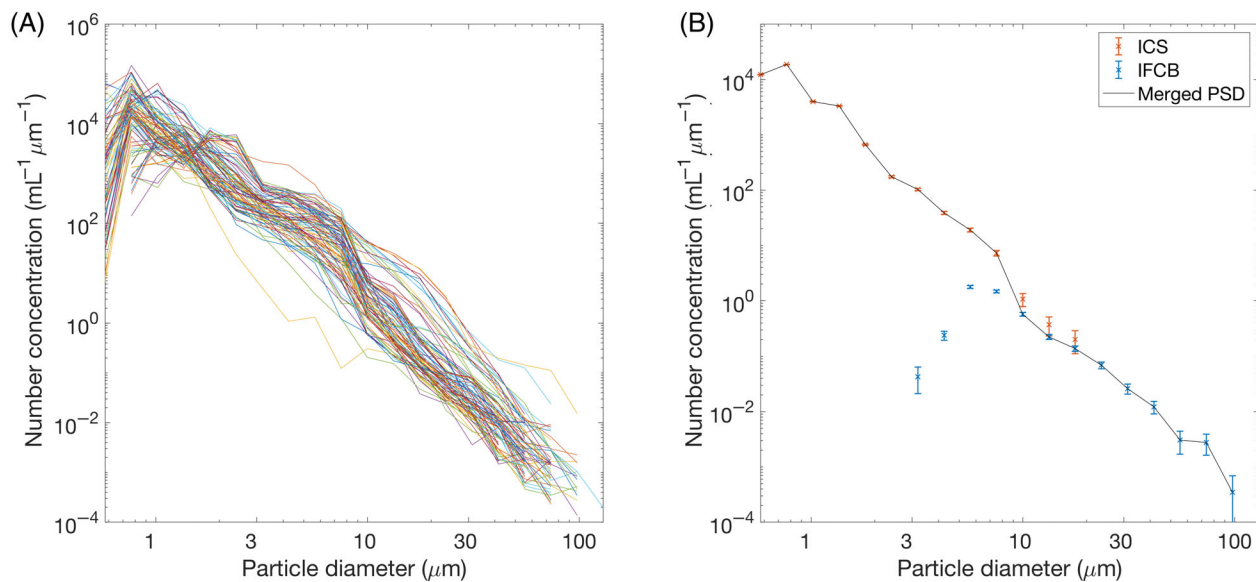


Fig 2. (A) Particle size distributions of all merged ICS and IFCB spectra and (B) one typical spectrum with calculated uncertainties. Uncertainties are calculated using particle counting errors that assume a Poisson distribution. The spectrum in panel (B) is sample 15 (Supporting Information Table S1), from 21 November 2015 (NA01), 43.4°N, -40.4°W, Chl a = 0.36 mg m⁻³.

and ICS to determine the threshold for accurate enumeration of nanoplankton cells by the IFCB (Fig. 2A). Counting efficiency of the IFCB begins to decrease for particles below 6–9 μ m. We identified the point of the start of this decrease as the minimum size at which the IFCB provides quantitative information on particle concentrations (Fig. 2B). This minimum size threshold changes with instrument gain settings, and potentially also with the physiology of phytoplankton populations. We calculate and apply size thresholds based on threshold averages calculated for each cruise, using 6.3, 7.9, 8.8, and 7.1 μ m for the four chronological NAAMES cruises, respectively. Nanoplankton were thus estimated for each sample using the combined ICS data below these size thresholds and IFCB data above these size thresholds for each cruise.

IFCB and ICS samples were considered to be colocated if the time difference between the two did not exceed 3 h. Larger phytoplankton are less abundant for a given sample volume and therefore there is a higher uncertainty in their count compared to small cells. To address this bias, and to increase statistical power for counts of large cells, we used the following method: if the nearest matching IFCB sample had fewer than 2500 images, additional IFCB samples were added until a minimum of 2500 images were available for analysis, as long as the timeframe between ICS and IFCB sampling times did not exceed ± 3 h. To avoid combining in-line IFCB samples that were collected as the ship passed through different water masses, we removed any samples that deviated from the colocated IFCB/ICS sample by more than 36% in terms of the number of IFCB images per sample. This 36% threshold was determined by the value of the 84th percentile (equivalent to 1 SD above the mean for a normal distribution) of the

coefficient of variation of cell counts per sample for all samples within a maximum of ± 3 h of the nearest matching ICS and IFCB sample in time. This approach is motivated by the fact that, although there is some natural variability in cell counts within a given water mass, change in cell counts outside the 84th percentile may indicate the transition of the ship into a new water mass. This criterion resulted in the elimination of 75 out of 450 initial IFCB samples (17%) for a total of 375 remaining IFCB samples. We also visually checked the temperature and Chl a measured in surface waters across each given set of combined IFCB samples to confirm that the ship had not crossed biological and/or physical fronts during this time window. The end result of matching IFCB samples with coincident ICS samples is a data set of 90 IFCB/ICS matches with cellular biovolume and carbon estimates across all three PSCs. Finally, IFCB/ICS pairs were matched with corresponding HPLC samples. Sixty-five of the HPLC and ICS water samples were collected within 1 h of each other, and the remaining 25 within 3 h of each other. Total cell biovolumes obtained from cytometry were compared to HPLC-determined Chl a concentrations to assess how well the cytometry data represent the phytoplankton biomass at a given time and place (Fig. 3A). Cytometry cell carbon was converted to units of Chl a by applying the mean carbon-to-chlorophyll (C : Chl) values derived from two sources: (1) the photoacclimation model (PaM) of Behrenfeld et al. (2016) applied to the NAAMES data by Fox et al. (2020), and (2) the in-line measurements of particulate backscattering [$b_{bp}(\lambda)$] converted to phytoplankton carbon following Graff et al. (2015) and divided by Chl a concentrations, where Chl a is derived from particulate absorption [$a_p(\lambda)$] red peak line height as in Boss

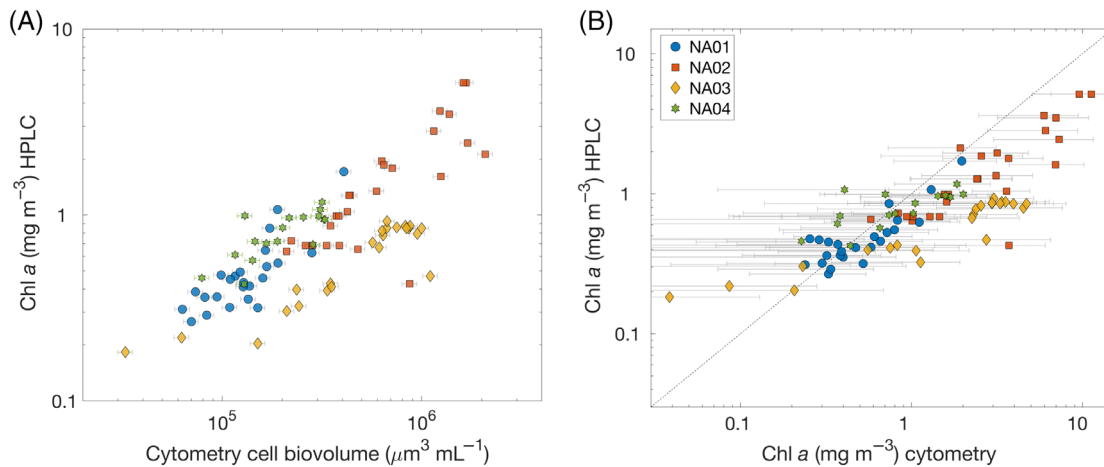


Fig 3. (A) Total cell biovolume from cytometry and Chl *a* concentration from HPLC across all 90 match-up samples. Y-axis error bars are the relative coefficient of variation in Chl *a* from HPLC based on replicate samples. X-axis error bars are based on 17% uncertainty in IFCB biovolume as estimated by Moberg and Sosik (2012) combined with cell counting uncertainties based on a Poisson distribution. In both panels, marker shapes represent the different NAAMES cruises. **(B)** Chl *a* estimated from cytometry data following conversion of cell biovolume to cell carbon and then to Chl. Y-axis error bars are as in (A), and x-axis error bars depict the range of Chl *a* values possible based on published C : Chl values (Sathyendranath et al. 2009).

et al. (2013). Data for $a_p(\lambda)$ and $b_{bp}(\lambda)$ are available at the NASA SeaBASS data repository (DOI: 10.5067/SeaBASS/NAAMES/DATA001). The C : Chl values from both the model and in-line data were calculated for each of the 90 points (Supporting Information Fig. S2), and range in value from 21 to 146 (model) and 14 to 139 (in-line data). While we obtained the best guess values of C : Chl from the two published approaches, there is still uncertainty in the accuracy of the conversion from carbon to Chl *a*. To show this uncertainty, we use minimum and maximum values of C : Chl from the literature, estimated as 15 and 176, respectively (Sathyendranath et al. 2009) and calculate the range of Chl *a* converted from cell carbon to estimate uncertainties (Fig. 3B). This range of possible C : Chl values is also used to show closure between the two measurement types (HPLC and cytometry). Contributions of the three phytoplankton size fractions to Chl *a* as derived from the DPA and cytometry approaches were compared using Pearson's linear correlation coefficient (r) and four additional metrics: absolute and relative root mean square error (RSME and rRMSE, respectively) and absolute and relative bias (see Supporting Information for equations).

Assessment and discussion

Overall trends in PSC estimate comparisons

Cell biovolumes from cytometry and Chl *a* concentrations from HPLC covary across all four cruises (Fig. 3A). Variability around this relationship is expected as the result of variation in Chl *a* per cell volume that occurs among different phytoplankton taxa as well as growth conditions, for example, nutrients and light. For example, there is noticeably lower Chl *a* per cell for the majority of samples from the NA03 cruise, which took place in August–September (Fig. 3B). This is

likely to be the result of nutrient limitation and/or high light adaptation associated with a shallower mixed layer depth (MLD) during the late summer and fall in the North Atlantic Ocean (Fox et al. 2020). Application of C : Chl values estimated for each sample (Supporting Information Fig. S2) resulted in a Pearson's linear correlation coefficient of $r = 0.79$ between Chl *a* concentrations from HPLC and cytometry (Fig. 3B). This is within the range of possible C : Chl from published estimates applied as described above and there is good agreement between Chl *a* calculated from HPLC and cytometry. Chl_p, Chl_n, and Chl_m calculated from cytometry are all positively correlated with Chl *a* from HPLC, while trends in F_p , F_n , and F_m compared to Chl *a* from HPLC are not significant (Supporting Information Fig. S3).

The two DPA equations to estimate the Chl *a* fraction of picoplankton (Table 1, Eqs. 1, 2) show different trends when compared to cytometry (Fig. 4A). Equation 1 significantly overestimates the relative contribution of picoplankton to Chl *a* and Eq. 2 significantly underestimates the picoplankton fraction (Table 3). We found poor correlation between the nanoplankton fraction calculated from all three DPA equations (Table 1, Eqs. 3–5) and the nanoplankton fraction from cytometry (Fig. 4B; Table 3). For the majority of the match-ups, DPA estimates of the nanoplankton fraction were lower than those from cytometry. For the microplankton, Eqs. 6, 7 (Table 1) both overestimate the microplankton fraction and show low correlations with cytometry (Fig. 4C; Table 3). Chl *a* concentrations associated with each size class show the same bias patterns as the PSC fractions (Fig. 4D–F; Table 4). In most cases, correlations are higher when considering Chl *a* concentrations of the three size classes and in some cases the values of relative bias (reflecting over- or underestimation) are improved when considering Chl *a* concentrations of PSCs (Table 4).

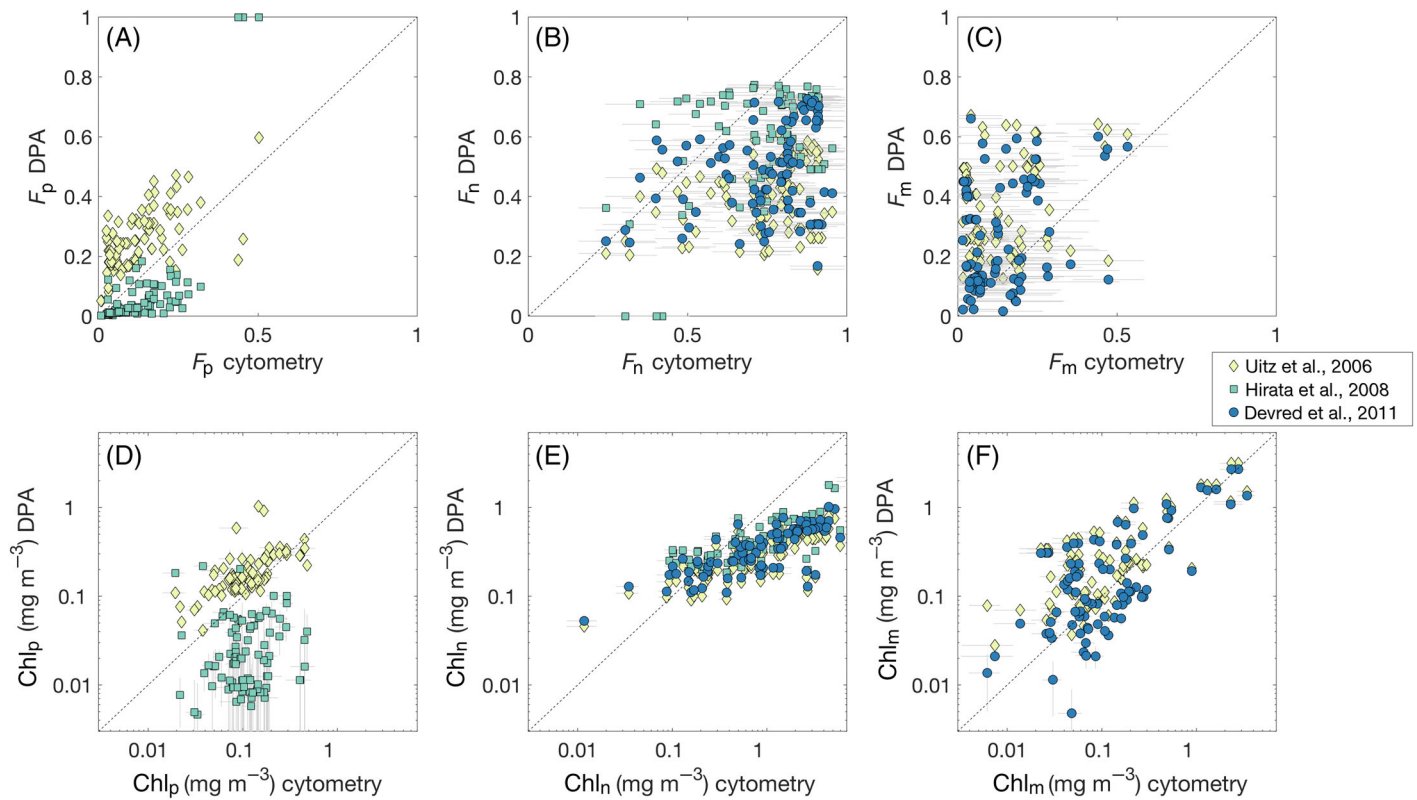


Fig 4. Fractions of (A) pico-, (B) nano-, and (C) microplankton calculated using cytometry (x-axes) and previously published DPA equations (y-axes; see Table 1 for equations). Error bars in the x-axis are determined by the propagated errors based on statistical counting uncertainties, estimation of cell biovolume, and the conversion between biovolume and cell carbon. (D–F) Chl *a* concentrations for each size class calculated from the DPA (y-axes) and cytometry (x-axes). Error bars in the y-axis represent the uncertainty in Chl *a* concentrations determined from replicate samples. X-axis error bars represent uncertainty calculated as in (A–C) x-axes, propagated with the uncertainty in the conversion from C : Chl based on the mean of values from the photoacclimation model and in-line bio-optical measurements.

Table 3. Statistics of PSC fractions estimated using published versions of the DPA compared to cytometry data. *r* denotes Pearson's linear correlation coefficient.

	Eq.	Reference	<i>r</i>	RMSE (unitless)	rRMSE (%)	Bias (unitless)	rBias (%)
F_p	(1)	Uitz et al. (2006)	0.58	0.15	94	0.13	79
	(2)	Hirata et al. (2008)	0.73	0.13	114	−0.05	−96
F_n	(3)	Uitz et al. (2006)	0.34	0.38	69	−0.34	−72
	(4)	Hirata et al. (2008)	0.35	0.26	38	−0.15	−20
	(5)	Devred et al. (2011)	0.35	0.32	54	−0.25	−72
F_m	(6)	Uitz et al. (2006)	0.31	0.28	116	0.21	96
	(7)	Devred et al. (2011)	0.34	0.23	102	0.12	61

Discrepancies between attribution of pigments to PSCs, and observed cell sizes and groups

A summary of the analysis on the discrepancies between pigment and size class assignments is shown in Table 5. Note that the lower size limit of the IFCB ($\sim 6\text{--}7\ \mu\text{m}$) allows for the identification of phytoplankton taxonomic groups within the nano- and microplankton size classes, but not the nanoplankton between 2 and 6 μm or the picoplankton size

class. Additionally, many cells $> 6\ \mu\text{m}$ are not identifiable in IFCB imagery due to the similarity in morphology of cells within several groups and image resolution. Table 5 also makes reference to cyanobacteria, which are not imaged by the IFCB in their single-celled form but are identified by the ICS. *Trichodesmium* colonies can be imaged by the IFCB, but their geographic range is limited to latitudes lower than those covered in this study. In our assessment of the

Table 4. Statistics of PSC Chl *a* concentrations estimated using published versions of the DPA compared to cytometry data. *r* denotes Pearson's linear correlation coefficient.

	Eq.	Reference	<i>r</i> *	RMSE (unitless)	rRMSE (%)	Bias (unitless)	rBias (%)
Chl _p	(1) × Chl <i>a</i>	Uitz et al. (2006)	0.67	0.15	60	0.07	44
	(2) × Chl <i>a</i>	Hirata et al. (2008)	0.09	0.13	136	−0.10	−119
Chl _n	(3) × Chl <i>a</i>	Uitz et al. (2006)	0.76	1.81	112	−1.19	−101
	(4) × Chl <i>a</i>	Hirata et al. (2008)	0.75	1.59	90	−0.94	−62
	(5) × Chl <i>a</i>	Devred et al. (2011)	0.75	1.65	100	−1.04	−81
Chl _m	(6) × Chl <i>a</i>	Uitz et al. (2006)	0.68	0.37	97	0.13	65
	(7) × Chl <i>a</i>	Devred et al. (2011)	0.62	0.35	95	0.05	27

*Calculation of *r* performed on the log-transformed Chl *a* data.

Table 5. Assignments of the seven accessory pigments used in the DPA to phytoplankton groups and size classes. Open boxes with dashed outlines indicate where groups are known to fall within the picoplankton size range but are not observed by the IFCB, which only quantifies cells approximately greater than 6–7 μm .

Diagnostic pigment	Abbreviation	Phytoplankton group(s)	Pico*	Nano*	Micro
Fucoxanthin	Fuco	Diatoms, Prymnesiophytes, Silicoflagellates			
Peridinin	Peri	Dinoflagellates			
19'-Hexanoyloxy-fucoxanthin	Hexa	Prymnesiophytes			
19'-Butanoyloxy-fucoxanthin	Buta	Prymnesiophytes, Silicoflagellates			
Alloxanthin	Allo	Cryptophytes			
TChlb	TChlb	Euglenoids, chlorophytes			
Zeaxanthin	Zea	Cyanobacteria†			

= DPA-based pigment size class assignments.

= Cell sizes of phytoplankton groups observed with IFCB imagery.

*Cyanobacteria, picoeukaryotes, and nanoplankton < 6–7 μm are not measured by the IFCB. These groups were sampled with the ICS; however, individual cell size of phytoplankton groups estimated by manual gating of ICS data were not analyzed in this study.

†Note that some cyanobacteria colonies, such as that of *Trichodesmium*, can reach microplankton size or larger.

discrepancies between pigments assigned to PSCs by the DPA approach and the observed size distributions of phytoplankton groups, we use ESD_V to define cell size (Fig. 5; Supporting Information Table S2). The use of ESD_V (vs., for example, cell major axis length) is appropriate as carbon and chlorophyll concentrations, which are the parameters used to represent phytoplankton biomass, are estimated from biovolume.

Picoplankton are defined by Uitz et al. (2006) as the weighted sum of TChlb and Zea, and by Hirata et al. (2008) as the weighted value of Zea alone plus all samples with Chl *a* concentrations < 0.25 mg m^{-3} (Table 1, Eqs. 1, 2, respectively). The result of this approach is an overestimation of picoplankton when all TChlb is assigned to the picoplankton

size class, and an underestimation when Zea alone is assigned to picoplankton (Fig. 4A,D). Zea is found primarily in cyanobacteria, which usually exist as picoplankton. TChlb is found in eukaryotic picoplankton, such as representative members of the phylum Chlorophyta (and more specifically some prasinophytes) (Jeffrey et al. 2011). However, TChlb-containing phytoplankton groups, namely euglenoids and chlorophytes, belonging to both the nanoplankton and microplankton size classes were detected in IFCB images (Figs. 5, 6). Note that the “unidentifiable” group in Figs. 5, 6 may also include TChlb-containing cells. Thus, it is not surprising that when all TChlb is assigned to picoplankton (Eq. 2), the DPA will overestimate the relative contribution of picoplankton. Other groups that contain neither Zea or TChlb

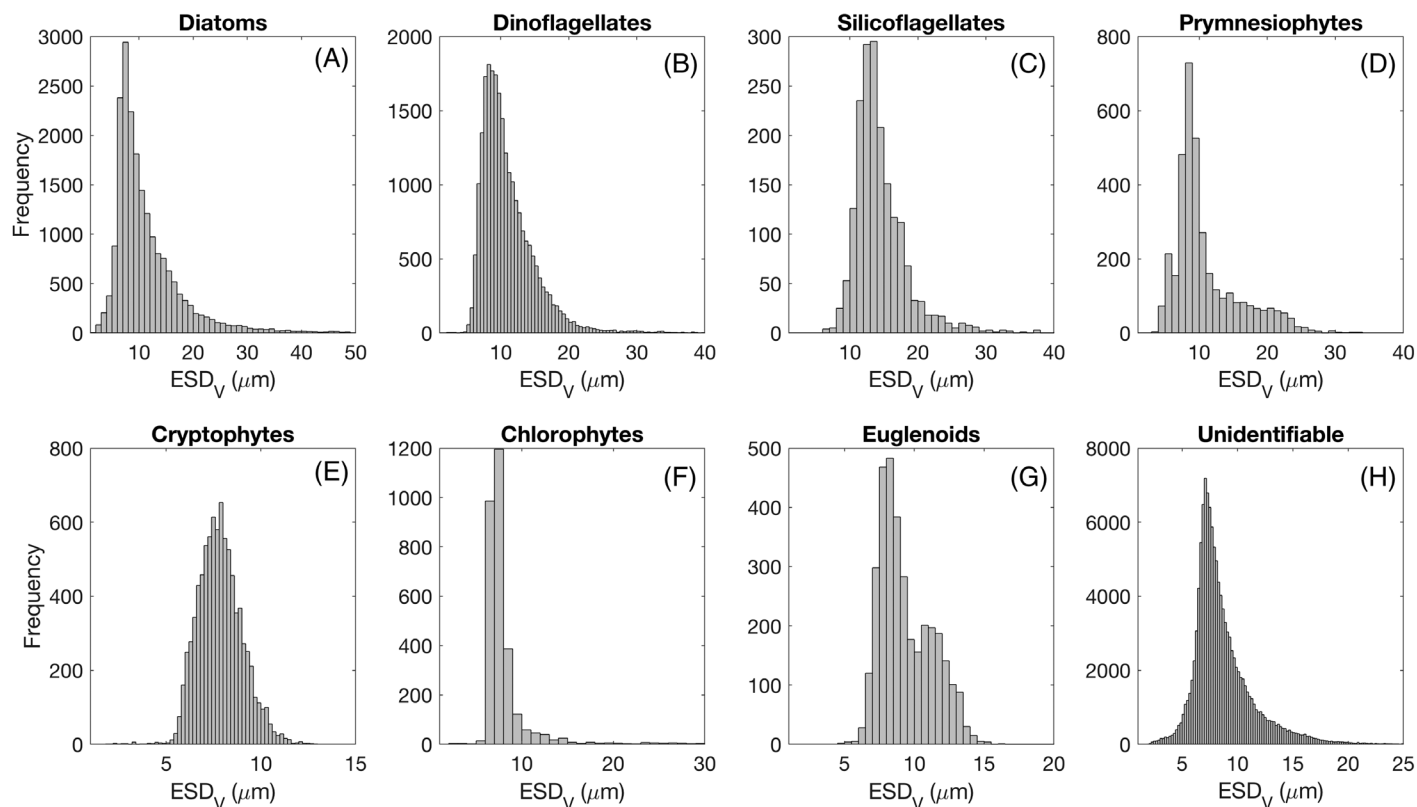


Fig 5. Frequency distributions of the equivalent spherical diameter determined from biovolume (ESD_V) of all imaged cells that have taxonomic assignment (panels **A–G**) and all unidentified cells (panel **H**). ESD_V is calculated from biovolume estimates of each cell imaged with the IFCB following Moberg and Sosik (2012). Note different ranges for x-axes.

but could be contributors to the picoplankton community include prymnesiophytes (Moon-Van Der Staay et al. 2000) and bolidophytes (Guillou et al. 1999; Kuwata et al. 2018).

The presence of nanoplankton is defined by the DPA as either the weighted sum of Allo, Buta, and Hexa (Table 1, Eq. 3); the same combination of pigments plus TChlb (Table 1, Eq. 4); or as in Eq. 3 but with some proportion of the Fuco reallocated from microplankton to nanoplankton (Table 1, Eq. 5). Allo is a diagnostic pigment for cryptophytes, which we observed in the nanoplankton size class in IFCB imagery (Fig. 4). Buta is found in prymnesiophytes such as *Phaeocystis* and coccolithophores, which are known to span all three size classes (Jeffrey et al. 1997; Jeffrey et al. 2011) and within our IFCB imagery data are observed both within nano- and microplankton size classes (Figs. 5, 6). Hexa is also found in prymnesiophytes, as well as in silicoflagellates (e.g., Dictyochaes) and pelagophytes. Dictyochaes are identifiable in IFCB imagery and fall within both the nano- and microplankton size classes (Figs. 5, 6; shown with label of silicoflagellates). TChlb, assigned by Eq. 4 to nanoplankton, is found in chlorophytes and euglenoids. However, among chlorophytes, prasinophytes are known as important members of the picoplankton (Jeffrey et al. 2011), and although rare, we also observed some microplankton-sized chlorophytes (Figs. 5, 6). Previous versions of the DPA generally overlook the contribution of

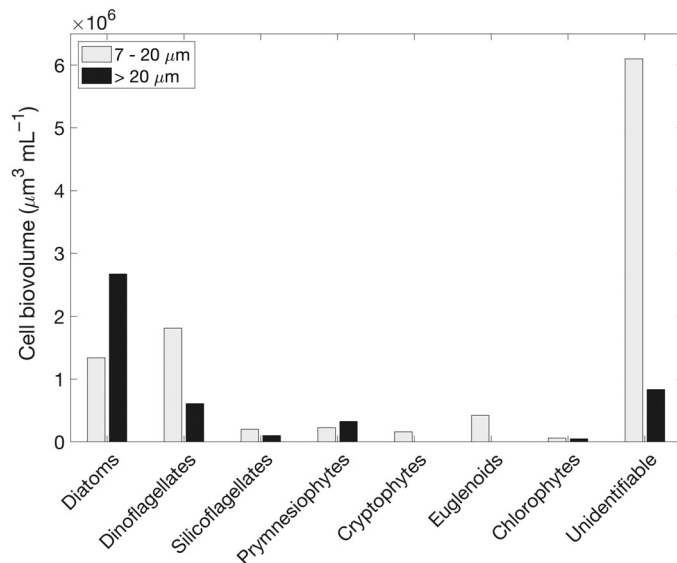


Fig 6. Summed biovolumes of phytoplankton taxa imaged by the IFCB across all samples analyzed in this study. Note that many dinoflagellates as well as some prymnesiophytes and cryptophytes have been identified, but because they are often more difficult to identify with high certainty, some cells of these types were classified as “unidentifiable” and hence biovolumes of these groups are likely to be underestimated. The “unidentifiable” category may also include other nanoeukaryote groups such as chlorophytes and pelagophytes.

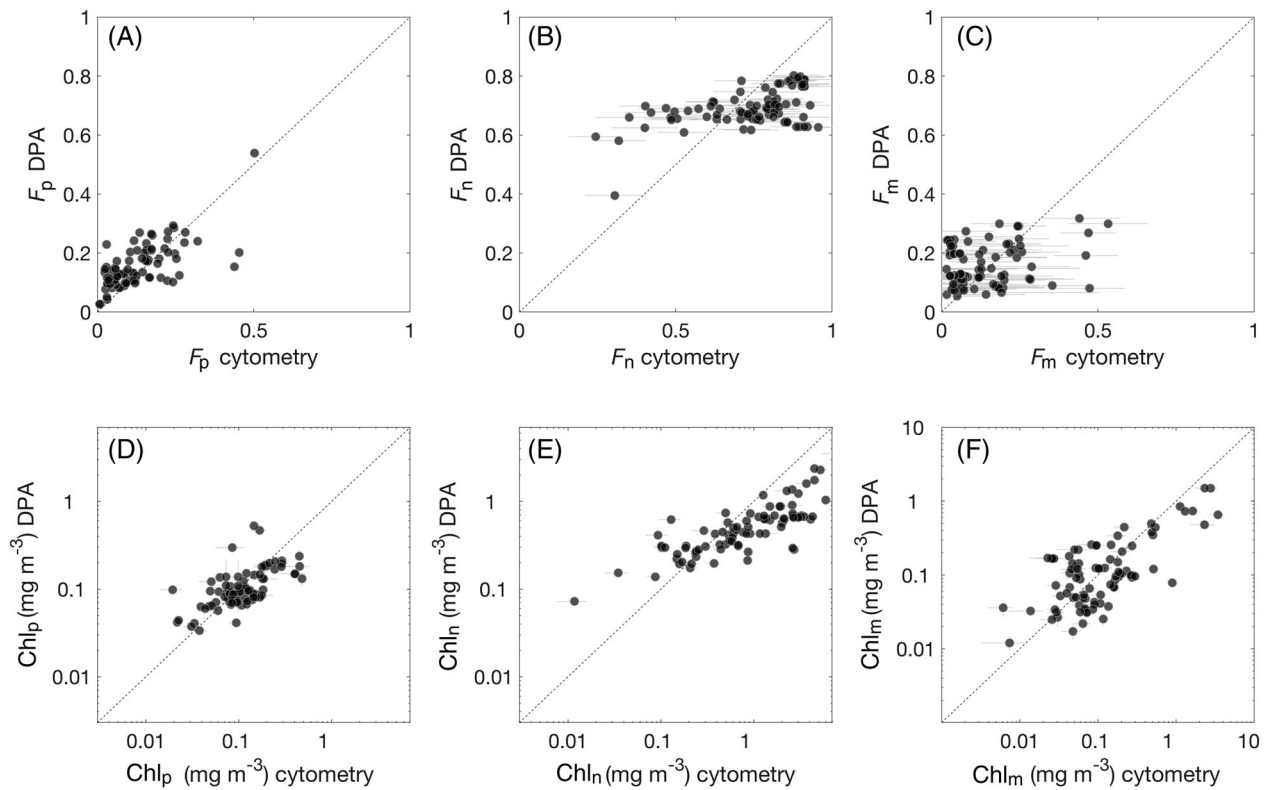


Fig 7. (A–C) Fractions of pico-, nano-, and microplankton, respectively, calculated using cytometry (x-axis) and Eqs. 8–10 (y-axis). Error bars in the x-axis direction are determined by the propagated errors based on statistical counting uncertainties, estimation of cell biovolume, and the conversion between biovolume and cell carbon. (D–F) Chl *a* concentrations for each size class calculated from Eqs. 8–10 (y-axes) \times HPLC Chl *a*, and cytometry (x-axes). Error bars in the y-axis direction represent the uncertainty in Chl *a* concentrations determined from replicate samples. X-axis error bars represent uncertainty calculated as in (A–C) x-axes, propagated with the uncertainty in the conversion from C : Chl based on the mean of values from the PaM model and inline bio-optical measurements.

diatoms to the nanoplankton. However, diatoms are known to span both the nanoplankton and microplankton size classes (Armbrust 2009), and the importance of nanoplankton diatoms has been recently highlighted (Leblanc et al. 2018). Our imagery data show that 33% of all diatom biovolume for cells $> 7 \mu\text{m}$ falls within the nanoplankton size class. This result is likely an underestimation of nanoplankton diatom biovolume due both to the possibility of unidentified cells in the IFCB imagery and/or the presence of diatoms below our defined IFCB detection limit for each cruise (6.3–8.8 μm). We also note that chain-forming taxa such as *Chaetoceros* are evaluated for cell size by summing the biovolume of all cells in the chain and not by treating each cell individually. Prymnesiophytes and silicoflagellates also both span the nano- and microplankton size ranges and contain Fuco. Devred et al. (2011) assume Hexa and Buta are only present in the nanoplankton size class, and the relationship between Hexa, Buta, and Fuco is then used to attribute some proportion of Fuco to nanoplankton rather than microplankton. Applying the adjustment to the DPA by Devred et al. (2011) to account for the Fuco present within nanoplankton attributes, on average, 44% ($\pm 29\%$ SD) of the Fuco in our dataset to nanoplankton. Microplankton are overestimated by the DPA (Table 1, Eqs. 6, 7) when defined as

the weighted sum of all Fuco and Peri (Eq. 6) or when defined by the weighted sum of all Peri and the remaining fraction of Fuco not attributed to nanoplankton (Eq. 7; Fig. 4C,F). Of identifiable dinoflagellates, we observe 74% of cell biovolume within the 7–20 μm nanoplankton size class (Fig. 5). This result is notable in its indication that DPA equations are incorrectly assigning Peri, found exclusively in dinoflagellates, to the microplankton (Table 1, Eqs. 6, 7). However, we also note the significant portion of unassigned cells (unidentifiable) in the IFCB data. These cells may be a driving factor in the poor representation of PSCs by DPA pigments in this data set, but without taxonomic identification we are unable to determine which diagnostic pigments the unidentifiable cells contain.

Overall, identification of nano- and microplankton cells using IFCB imagery reveals the extent to which several major phytoplankton groups are mis-assigned to size classes by the DPA framework. Although previous work on development of the DPA has often acknowledged its assumptions and potential sources of uncertainty, we now have the cytometry and taxonomy data needed to address how these assumptions impart biases to estimated PSCs. Most notably, the attribution of all Peri (found in dinoflagellates) to microplankton by all

Table 6. Statistics of PSC fractions and Chl *a* concentrations estimated using updated DPA equations (Eqs. 8–10, this study) compared to cytometry data. *r* denotes Pearson's linear correlation coefficient.

	Eq.	<i>r</i>	RMSE (unitless)	rRMSE (%)	Bias (unitless)	rBias (%)
F_p	(8)	0.70	0.07	63	0.03	38
F_n	(9)	0.51	0.13	19	−0.06	−6
F_m	(10)	0.20	0.12	86	0.03	38
Chl _p	(8) × Chl <i>a</i>	0.66*	0.09	44	−0.01	−7
Chl _n	(9) × Chl <i>a</i>	0.84*	1.40	78	−0.87	−49
Chl _m	(10) × Chl <i>a</i>	0.65*	0.42	84	−0.10	−3

*Calculation of *r* for Chl *a* concentrations performed on the log-transformed Chl *a* data.

published DPA microplankton equations, as well as the attribution of TChlb to picoplankton in the most commonly applied version of the DPA from Uitz et al. (2006), results in biased PSC fractions and PSC Chl *a* concentrations. The presence of pigments in size classes other than what is defined by the DPA was also shown by Uitz et al. (2009) (see their Fig. 2). The authors observed 67% of Fuco in the 2–10 μm Chl *a* fraction, and the three pigments assigned to nanoplankton by the DPA (Hexa, Buta, and Allo) in all three of the 0.4–2, 2–10, and > 10 μm Chl *a* size fractions. We also note that for practical reasons, such as filter pore size as in Uitz et al. (2009), size cut-offs other than 2 and 20 μm are used in studies of phytoplankton community size structure.

Recommendations

As a result of the direct comparisons between DPA results and cytometry data presented in this study, we recommend a set of DPA equations for estimating PSCs informed by technological advances that provide single cell metrics spanning the full size range of phytoplankton. Based on the presence of accessory pigments in major phytoplankton groups (Jeffrey et al. 1997; Jeffrey et al. 2011) and the size ranges of phytoplankton groups from the literature and as observed in this study, several adjustments are suggested regarding the assumptions of current DPA methods. Our recommendation is based on a qualitative evaluation of our pigment assignments using the cytometry data of our study and provides new DPA equations that are quantitatively determined to be unbiased for our study area in the western North Atlantic. While our data are regional, the assignment of pigments to PSCs is not specific to groups found within the North Atlantic and requires evaluation for use in other regions of the globe. However, previously published DPA equations evaluated here were derived in specific regions, including the original assignment of diagnostic pigments to taxa and size classes derived from Mediterranean Sea data (Vidussi et al. 2001).

We define the fraction of picoplankton as the weighted sum of Zea and half of the TChlb to account for the presence of TChlb in both pico- and nanoplankton (Eq. 8). Although some TChlb-containing groups can be microplankton,

including some euglenoids and the chlorophytes *Halosphaera* and *Pterosperma*, we observed these infrequently. As such, we distribute the TChlb between pico- and nanoplankton, which contain common marine genera including *Micromonas*, *Prymnomonas*, and other prasinophytes, as well as *Euglena* and *Pterosperma* (Thronsdon 1997). The nanoplankton fraction is defined by the weighted sum of Hexa, Buta, and Allo, the remaining half of TChlb, half of the Fuco concentration, and 75% of the total Peri concentration (Eq. 9). The assignments of Hexa, Buta, and Allo to nanoplankton are unchanged from previously published DPA equations. Microplankton-sized prymnesiophytes and silicoflagellates that may contain Hexa and Buta were present in our samples; the potential for prymnesiophytes in both the unidentifiable nanoplankton category and in the picoplankton renders it difficult to know how to accurately redistribute Hexa or Buta out of nanoplankton. The microplankton fraction is defined as the weighted sum of the remaining half of the Fuco combined with the remaining 25% of Peri (Eq. 10).

$$F_p = \frac{0.5W_6P_6 + W_7P_7}{DP_w} \quad (8)$$

$$F_n = \frac{0.5W_1P_1 + 0.75W_2P_2 + \sum_{i=3}^5 W_iP_i + 0.5W_6P_6}{DP_w} \quad (9)$$

$$F_m = \frac{0.5W_1P_1 + 0.25W_2P_2}{DP_w} \quad (10)$$

For consistency, we evaluate Eqs. 8–10 using the pigment weighting values (*W*) from Uitz et al. (2006) against performance metrics of Eqs. 1–7. We also tested values of *W* derived from our North Atlantic data set and the results we observed (Fig. 7; Table 6) were not significantly different. Results show improved relationships for all three size classes, both in relative fractions and in Chl *a* concentrations (Fig. 7; Table 6). In particular, the values of absolute and relative bias are reduced in all cases and is an improvement even when overall uncertainty due to natural variability cannot be eliminated. Despite reallocated pigments and adjusted DPA equations, there is a clear fractionation of phytoplankton into size classes by the DPA, whereas the cytometry data displays

a continuum. For example, Fig. 7B shows the Chl *a* fraction of nanoplankton mainly falling within the range of 60–80% while the Chl *a* fraction of nanoplankton from cytometry spans 20–100%.

The simplified proportions of pigments allocated to each size class by the updated DPA method presented here cannot represent the complexity that underlies the allocation of pigments to phytoplankton groups and size classes in the ocean. However, we have shown that with several simple adjustments some of the biases of current DPA methods are reduced. Still, it is important to consider how natural variability may impact the interpretation of results derived using the DPA approach. For the purpose of identifying the contribution of Chl *a* to the three size classes, the DPA may be a reasonable approach, as size fractionated Chl *a* was found to agree well with DPA Chl *a* size fractions (Brewin et al. 2014). However, for estimates of phytoplankton biomass, as are often implied to be determined by the DPA in the literature, the direct evaluation of phytoplankton biomass to PSCs presented here indicates the DPA requires careful interpretation if it is to be used for these purposes.

In addition to recommending the use of Eqs. 8–10 to estimate PSCs, we also encourage the application of uncertainties when calculating estimated PSC fractions or Chl *a* concentrations. This article provides quantified uncertainties associated with previously published DPA equations (Tables 3, 4), as well as for the new equations presented here (Eq. 8–10; Table 6) when evaluated against cytometry-based PSCs. With the rapid advancement of technology for quantifiable measurements of plankton (Lombard et al. 2019), we recommend the use of multiple approaches that independently evaluate phytoplankton biomass within different size classes and provide uncertainty across a broad range of oceanographic conditions. As the DPA is applied to future studies of ocean ecosystems, satellite algorithm development, and ecosystem models, its inherent biases and uncertainties must be considered.

References

- Armbrust, E. V. 2009. The life of diatoms in the world's oceans. *Nature* **459**: 185–192. doi:[10.1038/nature08057](https://doi.org/10.1038/nature08057)
- Behrenfeld, M. J., and others. 2016. Reevaluating ocean warming impacts on global phytoplankton. *Nat. Clim. Chang.* **6**: 323–330. doi:[10.1038/nclimate2838](https://doi.org/10.1038/nclimate2838)
- Behrenfeld, M. J., and others. 2019. The North Atlantic Aerosol and Marine Ecosystem Study (NAAMES): Science motive and mission overview. *Front. Mar. Sci.* **6**: 122. doi:[10.3389/fmars.2019.00122](https://doi.org/10.3389/fmars.2019.00122)
- Boss, E., and others. 2013. The characteristics of particulate absorption, scattering and attenuation coefficients in the surface ocean; contribution of the Tara Oceans expedition. *Methods Oceanogr.* **7**: 52–62. doi:[10.1016/j.mio.2013.11.002](https://doi.org/10.1016/j.mio.2013.11.002)
- Brewin, R. J., and others. 2011. An intercomparison of bio-optical techniques for detecting dominant phytoplankton size class from satellite remote sensing. *Remote Sens. Environ.* **115**: 325–339. doi:[10.1016/j.rse.2010.09.004](https://doi.org/10.1016/j.rse.2010.09.004)
- Brewin, R. J., S. Sathyendranath, T. Jackson, R. Barlow, V. Brotas, R. Aïrs, and T. Lamont. 2015. Influence of light in the mixed-layer on the parameters of a three-component model of phytoplankton size class. *Remote Sens. Environ.* **168**: 437–450. doi:[10.1016/j.rse.2015.07.004](https://doi.org/10.1016/j.rse.2015.07.004)
- Brewin, R. J. W., S. Sathyendranath, T. Hirata, S. J. Lavender, R. M. Barciela, and N. J. Hardman-Mountford. 2010. A three-component model of phytoplankton size class for the Atlantic Ocean. *Ecol. Model.* **221**: 1472–1483. doi:[10.1016/j.ecolmodel.2010.02.014](https://doi.org/10.1016/j.ecolmodel.2010.02.014)
- Brewin, R. J. W., S. Sathyendranath, G. Tilstone, P. K. Lange, and T. Platt. 2014. A multicomponent model of phytoplankton size structure. *J. Geophys. Res. Oceans* **119**: 1–19. doi:[10.1002/2014JC009859](https://doi.org/10.1002/2014JC009859)
- Brewin, R. J. W., and others. 2017. Uncertainty in ocean-color estimates of chlorophyll for phytoplankton groups. *Front. Mar. Sci.* **4**: 104. doi:[10.3389/fmars.2017.00104](https://doi.org/10.3389/fmars.2017.00104)
- Brotas, V., and others. 2013. Deriving phytoplankton size classes from satellite data: Validation along a trophic gradient in the eastern Atlantic Ocean. *Remote Sens. Environ.* **134**: 66–77. doi:[10.1016/j.rse.2013.02.013](https://doi.org/10.1016/j.rse.2013.02.013)
- Chisholm, S. W. 1992. Phytoplankton size, p. 213–237. *In* P. G. Falkowski, A. D. Woodhead, and K. Vivirito [eds.], *Primary productivity and biogeochemical cycles in the sea*. Springer.
- Claustre, H. 1994. The trophic status of various oceanic provinces as revealed by phytoplankton pigment signatures. *Limnol. Oceanogr.* **39**: 1206–1210. doi:[10.4319/lo.1994.39.5.1206](https://doi.org/10.4319/lo.1994.39.5.1206)
- Della Penna, A., and P. Gaube. 2019. Overview of (sub)meso-scale ocean dynamics for the NAAMES field program. *Front. Mar. Sci.* **6**: 384. doi:[10.3389/fmars.2019.00384](https://doi.org/10.3389/fmars.2019.00384)
- Devred, E., S. Sathyendranath, V. Stuart, and T. Platt. 2011. A three component classification of phytoplankton absorption spectra: Application to ocean-color data. *Remote Sens. Environ.* **115**: 2255–2266. doi:[10.1016/j.rse.2011.04.025](https://doi.org/10.1016/j.rse.2011.04.025)
- Di Cicco, A., M. Sammartino, S. Marullo, and R. Santoleri. 2017. Regional empirical algorithms for an improved identification of phytoplankton functional types and size classes in the Mediterranean Sea using satellite data. *Front. Mar. Sci.* **4**: 126. doi:[10.3389/fmars.2017.00126](https://doi.org/10.3389/fmars.2017.00126)
- DuRand, M. D., R. J. Olson, and S. W. Chisholm. 2001. Phytoplankton population dynamics at the Bermuda Atlantic Time-series station in the Sargasso Sea. *Deep-Sea Res. Part II Top. Stud. Oceanogr.* **48**: 1983–2003. doi:[10.1016/S0967-0645\(00\)00166-1](https://doi.org/10.1016/S0967-0645(00)00166-1)
- Fox, J., and others. 2020. Phytoplankton growth and productivity in the Western North Atlantic: Observations of regional variability from the NAAMES field campaigns. *Front. Mar. Sci.* **7**: 1–15. doi:[10.3389/fmars.2020.00024](https://doi.org/10.3389/fmars.2020.00024)

- Gin, K. Y. H., S. W. Chisholm, and R. J. Olson. 1999. Seasonal and depth variation in microbial size spectra at the Bermuda Atlantic time series station. *Deep-Sea Res. Part I Oceanogr. Res. Pap.* **46**: 1221–1245. doi:[10.1016/S0967-0637\(99\)00004-7](https://doi.org/10.1016/S0967-0637(99)00004-7)
- Gittings, J. A., R. J. W. Brewin, D. E. Raitsos, M. Kheireddine, M. Ouhssain, B. H. Jones, and I. Hoteit. 2019. Remotely sensing phytoplankton size structure in the Red Sea. *Remote Sens. Environ.* **234**: 111387. doi:[10.1016/j.rse.2019.111387](https://doi.org/10.1016/j.rse.2019.111387)
- Graff, J. R., and others. 2015. Analytical phytoplankton carbon measurements spanning diverse ecosystems. *Deep-Sea Res. Part I Oceanogr. Res. Pap.* **102**: 16–25. doi:[10.1016/j.dsr.2015.04.006](https://doi.org/10.1016/j.dsr.2015.04.006)
- Graff, J. R., and M. J. Behrenfeld. 2018. Photoacclimation responses in subarctic Atlantic phytoplankton following a natural mixing-restratification event. *Front. Mar. Sci.* **5**: 209. doi:[10.3389/fmars.2018.00209](https://doi.org/10.3389/fmars.2018.00209)
- Guillou, L., M. J. Chrétiennot-Dinet, L. K. Medlin, H. Claustre, S. Loiseaux-de Goër, and D. Vaultot. 1999. Bolidomonas: A new genus with two species belonging to a new algal class, the Bolidophyceae (Heterokonta). *J. Phycol.* **35**: 368–381. doi:[10.1046/j.1529-8817.1999.3520368.x](https://doi.org/10.1046/j.1529-8817.1999.3520368.x)
- Hirata, T., J. Aiken, N. Hardman-Mountford, T. Smyth, and R. Barlow. 2008. An absorption model to determine phytoplankton size classes from satellite ocean colour. *Remote Sens. Environ.* **112**: 3153–3159. doi:[10.1016/j.rse.2008.03.011](https://doi.org/10.1016/j.rse.2008.03.011)
- Hirata, T., and others. 2011. Synoptic relationships between surface chlorophyll-*a* and diagnostic pigments specific to phytoplankton functional types. *Biogeosciences* **8**: 311–327. doi:[10.5194/bg-8-311-2011](https://doi.org/10.5194/bg-8-311-2011)
- Hooker, S. B., and others. 2009. The third SeaWiFS HPLC analysis round-robin experiment SeaHARRE-3. NASA/TM-2009–215849. December, 2009.
- Jeffrey, V. M., R. F. C. Mantoura, and S. W. Morgan. 1997. *Phytoplankton pigments in oceanography*. UNESCO.
- Jeffrey, S. W., S. W. Wright, M. Zapata, S. Roy, C. A. Llewellyn, E. S. Egeland, and G. Johnsen. 2011. *Microalgal classes and their signature pigments. Phytoplankton pigments: Characterization, chemotaxonomy and applications in oceanography*. New York, NY: Cambridge Univ. Press.
- Koestner, D., D. Stramski, and R. A. Reynolds. 2020. Assessing the effects of particle size and composition on light scattering through measurements of size-fractionated seawater samples. *Limnol. Oceanogr.* **65**: 173–190. doi:[10.1002/lno.11259](https://doi.org/10.1002/lno.11259)
- Kostadinov, T. S., D. A. Siegel, and S. Maritorena. 2009. Retrieval of the particle size distribution from satellite ocean color observations. *J. Geophys. Res. Oceans* **114**: 1–22. doi:[10.1029/2009JC005303](https://doi.org/10.1029/2009JC005303)
- Kostadinov, T. S., D. A. Siegel, and S. Maritorena. 2010. Global variability of phytoplankton functional types from space: Assessment via the particle size distribution. *Biogeosciences* **7**: 3239–3257. doi:[10.5194/bg-7-3239-2010](https://doi.org/10.5194/bg-7-3239-2010)
- Kramer, S. J., and D. A. Siegel. 2019. How can phytoplankton pigments be best used to characterize surface ocean phytoplankton groups for ocean color remote sensing algorithms? *J. Geophys. Res. Oceans* **124**: 7557–7574. doi:[10.1029/2019JC015604](https://doi.org/10.1029/2019JC015604)
- Kuwata, A., K. Yamada, M. Ichinomiya, S. Yoshikawa, M. Tragin, D. Vaultot, and A. L. dos Santos. 2018. Bolidophyceae, a sister picoplanktonic group of diatoms - a review. *Front. Mar. Sci.* **5**: 370. doi:[10.3389/fmars.2018.00370](https://doi.org/10.3389/fmars.2018.00370)
- Le Quere, C., and S. Harrison. 2005. Ecosystem dynamics based on plankton functional types for global ocean biogeochemistry models. *Glob. Chang. Biol.* **11**: 2016–2040. doi:[10.1111/j.1365-2486.2005.01004.x](https://doi.org/10.1111/j.1365-2486.2005.01004.x)
- Leblanc, K., and others. 2018. Nanoplanktonic diatoms are globally overlooked but play a role in spring blooms and carbon export. *Nat. Commun.* **9**: 1–12. doi:[10.1038/s41467-018-03376-9](https://doi.org/10.1038/s41467-018-03376-9)
- Li, Z., L. Li, K. Song, and N. Cassar. 2013. Estimation of phytoplankton size fractions based on spectral features of remote sensing ocean color data. *J. Geophys. Res. Oceans* **118**: 1445–1458. doi:[10.1002/jgrc.20137](https://doi.org/10.1002/jgrc.20137)
- Litchman, E., and C. A. Klausmeier. 2008. Trait-based community ecology of phytoplankton. *Annu. Rev. Ecol. Evol. Syst.* **39**: 615–639. doi:[10.1146/annurev.ecolsys.39.110707.173549](https://doi.org/10.1146/annurev.ecolsys.39.110707.173549)
- Litchman, E., P. de Tezanos Pinto, C. A. Klausmeier, M. K. Thomas, and K. Yoshiyama. 2010. Linking traits to species diversity and community structure in phytoplankton. *Hydrobiologia* **653**: 15–28. doi:[10.1007/s10750-010-0341-5](https://doi.org/10.1007/s10750-010-0341-5)
- Lombard, F., and others. 2019. Globally consistent quantitative observations of planktonic ecosystems. *Front. Mar. Sci.* **6**: 196. doi:[10.3389/fmars.2019.00196](https://doi.org/10.3389/fmars.2019.00196)
- Lorenzoni, L., G. Toro-Farmer, R. Varela, L. Guzman, J. Rojas, E. Montes, and F. Muller-Karger. 2015. Characterization of phytoplankton variability in the Cariaco Basin using spectral absorption, taxonomic and pigment data. *Remote Sens. Environ.* **167**: 259–268. doi:[10.1016/j.rse.2015.05.002](https://doi.org/10.1016/j.rse.2015.05.002)
- Mackey, M., D. Mackey, H. W. Higgins, and S. W. Wright. 1996. CHEMTAX - a program for estimating class abundances from chemical markers: Application to HPLC measurements of phytoplankton. *Mar. Ecol. Prog. Ser.* **144**: 265–283. doi:[10.3354/meps144265](https://doi.org/10.3354/meps144265)
- Menden-Deuer, S., and E. J. Lessard. 2000. Carbon to volume relationships for dinoflagellates, diatoms, and other protist plankton. *Limnol. Oceanogr.* **45**: 569–579. doi:[10.4319/lo.2000.45.3.0569](https://doi.org/10.4319/lo.2000.45.3.0569)
- Moberg, E. A., and H. M. Sosik. 2012. Distance maps to estimate cell volume from two-dimensional plankton images. *Limnol. Oceanogr.: Methods* **10**: 278–288. doi:[10.4319/lom.2012.10.278](https://doi.org/10.4319/lom.2012.10.278)
- Moon-Van Der Staay, S. Y., G. W. Van Der Staay, L. Guillou, D. Vaultot, H. Claustre, and L. K. Médlin. 2000. Abundance and diversity of prymnesiophytes in the picoplankton community from the equatorial Pacific Ocean inferred from 18S rDNA sequences. *Limnol. Oceanogr.* **45**: 98–109. doi:[10.4319/lo.2000.45.1.0098](https://doi.org/10.4319/lo.2000.45.1.0098)

- Mouw, C. B., and others. 2017. A consumer's guide to satellite remote sensing of multiple phytoplankton groups in the global ocean. *Front. Mar. Sci.* **4**: 41. doi:[10.3389/fmars.2017.00041](https://doi.org/10.3389/fmars.2017.00041)
- Nayar, S., and L. M. Chou. 2003. Relative efficiencies of different filters in retaining phytoplankton for pigment and productivity studies. *Estuar. Coast. Shelf Sci.* **58**: 241–248. doi:[10.1016/S0272-7714\(03\)00075-1](https://doi.org/10.1016/S0272-7714(03)00075-1)
- Olson, R. J., and H. M. Sosik. 2007. A submersible imaging-inflow instrument to analyze nano- and microplankton: Imaging FlowCytobot. *Limnol. Oceanogr.: Methods* **5**: 195–203. doi:[10.4319/lom.2007.5.195](https://doi.org/10.4319/lom.2007.5.195)
- Organelli, E., A. Bricaud, D. Antoine, and J. Uitz. 2013. Multivariate approach for the retrieval of phytoplankton size structure from measured light absorption spectra in the Mediterranean Sea (BOUSSOLE site). *Appl. Opt.* **52**: 2257–2273. doi:[10.1364/AO.52.002257](https://doi.org/10.1364/AO.52.002257)
- Picheral, M., S. Colin, and J.-O. Irisson. 2017. EcoTaxa, a tool for the taxonomic classification of images. Available from <https://ecotaxa.obs-vlfr.fr>. Accessed November 12, 2019
- Roy, S., S. Sathyendranath, H. Bouman, and T. Platt. 2013. The global distribution of phytoplankton size spectrum and size classes from their light-absorption spectra derived from satellite data. *Remote Sens. Environ.* **139**: 185–197. doi:[10.1016/j.rse.2013.08.004](https://doi.org/10.1016/j.rse.2013.08.004)
- Sathyendranath, S., and others. 2009. Carbon-to-chlorophyll ratio and growth rate of phytoplankton in the sea. *Mar. Ecol. Prog. Ser.* **383**: 73–84. doi:[10.3354/meps07998](https://doi.org/10.3354/meps07998)
- Sheldon, R. W., A. Prakash, and H. Sutcliffe. 1972. The size distribution of particles in the ocean. *Limnol. Oceanogr.* **17**: 327–340. doi:[10.4319/lo.1972.17.3.0327](https://doi.org/10.4319/lo.1972.17.3.0327)
- Sieburth, J. M., V. Smetacek, and J. Lenz. 1978. Pelagic ecosystem structure: Heterotrophic compartments of the plankton and their relationship to plankton size fractions. *Limnol. Oceanogr.* **23**: 1256–1263. doi:[10.4319/lo.1978.23.6.1256](https://doi.org/10.4319/lo.1978.23.6.1256)
- Sommer, U., K. Lengfellner, and A. Lewandowska. 2012. Experimental induction of a coastal spring bloom early in the year by intermittent high-light episodes. *Mar. Ecol. Prog. Ser.* **446**: 61–71. doi:[10.3354/meps09486](https://doi.org/10.3354/meps09486)
- Sommer, U., E. Charalampous, S. Genitsaris, and M. Moustaka-Gouni. 2017. Benefits, costs and taxonomic distribution of marine phytoplankton body size. *J. Plankton Res.* **39**: 494–508. doi:[10.1093/plankt/fbw071](https://doi.org/10.1093/plankt/fbw071)
- Soppa, M. A., T. Hirata, B. Silva, T. Dinter, I. Peeken, S. Wiegmann, and A. Bracher. 2014. Global retrieval of diatom abundance based on phytoplankton pigments and satellite data. *Remote Sens.* **6**: 10089–10106. doi:[10.3390/rs61010089](https://doi.org/10.3390/rs61010089)
- Sosik, H. M., and R. J. Olson. 2007. Automated taxonomic classification of phytoplankton sampled with imaging inflow cytometry. *Limnol. Oceanogr.: Methods* **5**: 204–216. doi:[10.4319/lom.2007.5.204](https://doi.org/10.4319/lom.2007.5.204)
- Thronsdon, J. and C. R. Tomas, 1997. The planktonic marine flagellates. Identifying marine phytoplankton. San Diego, CA: Academic Press.
- Uitz, J., H. Claustre, A. Morel, and S. B. Hooker. 2006. Vertical distribution of phytoplankton communities in open ocean: An assessment based on surface chlorophyll. *J. Geophys. Res.* **111**: C08005. doi:[10.1029/2005JC003207](https://doi.org/10.1029/2005JC003207)
- Uitz, J., Y. Huot, F. Bruyant, M. Babin, and H. Claustre. 2008. Relating phytoplankton photophysiological properties to community structure on large scales. *Limnol. Oceanogr.* **53**: 614–630. doi:[10.4319/lo.2008.53.2.0614](https://doi.org/10.4319/lo.2008.53.2.0614)
- Uitz, J., H. Claustre, F. B. Griffiths, J. Ras, N. Garcia, and V. Sandroni. 2009. A phytoplankton class-specific primary production model applied to the Kerguelen Islands region (Southern Ocean). *Deep-Sea Res. Part I Oceanogr. Res. Pap.* **56**: 541–560. doi:[10.1016/j.dsr.2008.11.006](https://doi.org/10.1016/j.dsr.2008.11.006)
- Van Heukelem, L., and C. S. Thomas. 2001. Computer-assisted high-performance liquid chromatography method development with applications to the isolation and analysis of phytoplankton pigments. *J. Chromatogr. A* **910**: 31–49. doi:[10.1016/S0378-4347\(00\)00603-4](https://doi.org/10.1016/S0378-4347(00)00603-4)
- Vidussi, F., H. Claustre, B. B. Manca, A. Luchetta, and J.-C. Marty. 2001. Phytoplankton pigment distribution in relation to upper thermocline circulation in the eastern Mediterranean Sea during winter. *J. Geophys. Res.* **106**: 19939–19956. doi:[10.1029/1999JC000308](https://doi.org/10.1029/1999JC000308)
- Zeng, C., S. Z. Rosengard, W. Burt, M. A. Peña, N. Nemcek, T. Zeng, K. R. Arrigo, and P. D. Tortell. 2018. Optically-derived estimates of phytoplankton size class and taxonomic group biomass in the eastern subarctic Pacific Ocean. *Deep-Sea Res. Part I Oceanogr. Res. Pap.* **136**: 107–118. doi:[10.1016/j.dsr.2018.04.001](https://doi.org/10.1016/j.dsr.2018.04.001)

Acknowledgments

Thanks to Michael Behrenfeld for conceptualization and leadership of the NAAMES expeditions and to the crew of the R/V *Atlantis* during all four NAAMES field campaigns. Thank you to Crystal Thomas at NASA Goddard Space Flight Center for analysis of HPLC samples, and to James Fox for providing calculated photoacclimation model C : Chl values. Thanks to Collin Roesler for helpful guidance and input on data analysis, and also to Heidi Sosik for helpful discussions regarding cytometry data and for making publicly available IFCB data processing codes (<https://github.com/hsosik/ifcb-analysis>). Data are available at EcoTaxa (<https://ecotaxa.obs-vlfr.fr/>) and the NASA SeaBASS repository (<https://seabass.gsfc.nasa.gov/>). We are extremely grateful to Aurea Ciotti, Bob Brewin, and one anonymous reviewer for their helpful comments that greatly improved the manuscript. Funding provided by NASA grants NNX15AE67G and NNX15AAF30G.

Conflict of Interest

None declared.

Submitted 16 January 2020

Revised 01 June 2020

Accepted 11 July 2020

Associate editor: Ivona Cetinic